SCIENTIFIC REPORTS
nature research

There are amendments to this paper

OPEN

Selective Priming of Tumor Blood Vessels by Radiation Therapy Enhances Nanodrug Delivery

Sijumon Kunjachan[1*], Shady Kotb[1,2], Robert Pola[4], Michal Pechar, Rajiv Kumar[1,3], Bijay Singh[3], Felix Gremse[5], Reza Taleeli[6], Florian Trichard, Vincent Motto-Ros[2], Lucie Sancey[7], Alexandre Detappe[1], Sayeda Yasmin-Karim[1], Andrea Protti[8], Ilanchezhian Shanmugam[3], Thomas Ireland[9], Tomas Etrych[4], Srinivas Sridhar[1,3], Olivier Tillement[2], Mike Makrigiorgos[1] & Ross I. Berbeco[1]

Effective drug delivery is restricted by pathophysiological barriers in solid tumors. In human pancreatic adenocarcinoma, poorly-permeable blood vessels limit the intratumoral permeation and penetration of chemo or nanotherapeutic drugs. New and clinically viable strategies are urgently sought to breach the neoplastic barriers that prevent effective drug delivery. Here, we present an original idea to boost drug delivery by selectively knocking down the tumor vascular barrier in a human pancreatic cancer model. Clinical radiation activates tumor endothelial-targeted gold nanoparticles to induce a physical vascular damage due to the high photoelectric interactions. *Active* modulation of these tumor neovessels lead to distinct changes in tumor vascular permeability. Noninvasive MRI and fluorescence studies, using a short-circulating nanocarrier with MR-sensitive gadolinium and a long-circulating nanocarrier with fluorescence-sensitive nearinfrared dye, demonstrate more than two-fold increase in nanodrug delivery, post tumor vascular modulation. Functional changes in altered tumor blood vessels and its downstream parameters, particularly, changes in K_{trans} (permeability), K_{ep} (flux rate), and V_e (extracellular interstitial volume), reflect changes that relate to augmented drug delivery. The proposed dual-targeted therapy effectively invades the tumor vascular barrier and improve nanodrug delivery in a human pancreatic tumor model and it may also be applied to other nonresectable, intransigent tumors that badly respond to standard drug therapies.

Drug delivery is limited by various pathophysiological barriers in solid tumors[1,2]. In human pancreatic adenocarcinoma (PDAC) – an aggressive form of cancer with a 5-year survival rate of 8.2%, drug therapies are impaired by hypopermeable tumor blood vessels, desmoplastic stroma, overexpression of growth factors, genetic mutations, altered signaling pathways and tumor heterogeneity[3–6]. With nearly a third of pancreatic cancer patients suffering from locally destructive disease, more potent and targeted interventions are highly essential[3]. A combination of rationally-designed chemotherapeutic and nanoparticle-based regimens have been shown to be beneficial in treating human pancreatic cancer. For instance, combination of gemcitabine and *nab*-paclitaxel have synergistically improved the clinical outcome for patients treated with advanced pancreatic cancer. It has been proposed that *nab*-paclitaxel increases the intratumoral accumulation of gemcitabine by degrading dense tumor stroma - a mechanism that is closely mimicked by hyaluronidase inhibitors[7]. Despite progressive advancements

[1]Department of Radiation Oncology, Brigham and Women's Hospital, Dana-Farber Cancer Institute and Harvard Medical School, Boston, MA, United States. [2]Institut Lumière Matière, UMR 5306, Université Claude Bernard Lyon 1, CNRS, Villeurbanne, France. [3]Nanomedicine Science and Technology Center and Department of Physics, Northeastern University, Boston, MA, United States. [4]Institute of Macromolecular Chemistry, Academy of Sciences of the Czech Republic, Heyrovsky Square 2, 16206, Prague 6, Czech Republic. [5]Experimental Molecular Imaging, University Hospital and Helmholtz Institute for Biomedical Engineering, RWTH Aachen University, Aachen, Germany. [6]Division of Medical Physics & Engineering, University of Texas Southwestern Medical Center, Texas, United States. [7]Institute for Advanced Biosciences, UGA/INSERM U1209/CNRS UMR 5309 Joint Research Center, Grenoble, France. [8]Lurie Family Imaging Center, Department of Radiology, Dana-Farber Cancer Institute and Harvard Medical School, Boston, MA, United States. [9]LA-ICP-MS and ICP-ES Laboratories, Department of Earth and Environmental Sciences, Boston University, Boston, MA, United States. *email: sijumon@gmail.com

in combination treatments, the limited delivery efficiency of these agents persists due to the pathophysiological limitations inherent in pancreatic tumors[3,6].

Clinical experience with routinely administered (nano) drugs including Doxil and/ or *nab*-Paclitaxel demonstrate improvements in reducing drug-related toxicities albeit with little therapeutic gain[7–10]. In fact, studies show that accumulation of (nano) drugs in human pancreatic tumor models is relatively low[3,5,11]. More innovative and clinically adaptable approaches are highly essential for effective drug delivery and prolonged survival in pancreatic cancer patients.

Tumor neovasculature form a major barrier to effective drug delivery[12–15]. It has been observed that even clonogenic cell death following radiation treatment is mediated by microvascular endothelial damage[16]. The presence of a dense tumor stroma comprised of collagen, fibroblasts, and hyaluronates impede the permeation and penetration of nanodrugs. However, this unique tumor physiology favour an opportunisitic targeting of tumor blood vessels by facilitating the pervascular retention of these radiosensitizing nanoparticles. Furthermore, the higher overexpression of integrin receptors in the tumor neoendothelium of slow-growing pancreatic models such as BxPC3, Capan1 *vs.* fast-growing Panc1 (or CT26, C26 colon cancer models) futher strengthens the rationale for tumor vascular-targeted radiation interventions[17].

High-*Z* metallic nanoparticles impart a local radiation boost during radiation therapy due to its increased photoelectric interactions[18–20]. Gold nanoparticles are safe, biocompatible, and therapeutically beneficial in moderate doses[21–25]. An LD50 of 3.2 g/kg has been reported in mice after its *i.v.* administration, with no long-term kidney toxicity, observed for 2.7 g/kg[18,26]. Ultrasmall nanoparticles of 1–5 nm are renally eliminated and cleared from the body *via* various phase degradation mechanisms[27,28]. Vascular targeting ligands such as cRGD (a cyclo-pentapeptide) has strong binding affinity to $\alpha_v\beta_3$ and $\alpha_v\beta_5$ integrin receptors present along the endothelial linings of *h*-PDAC[14,29]. When attached to the PEG functionalized gold core, these radiosensitizing nanoparticles circulate longer and anchor specifically to the tumor neoendothelium. Moreover, the dense stromal matrix of *h*-PDAC also lead to the perivascular retention of these nanoparticles and thereby invoking an indirect radiation response.

Tumor endothelial targeted gold nanoparticles (t-NP) can induce vascular modulation in *h*-PDAC during radiation therapy (RT)[14]. The sub-mm precision of modern clinical RT and the target-specificity of t-NP makes this a "dual-targeted" treatment with high spatiotemporal accuracy. Furthermore, we hypothesized that the local tumor vascular modulation induced by combined nanoparticle and radiation treatment (t-NP + RT) can improve tumor vascular permeability and facilitate targeted drug delivery. This is particularly significant in treating pancreatic tumors due to their poor tumor vascular permeability and critically low uptake of chemo or nanotherapeutic agents[11].

In this study, we demonstrate that nanodrug delivery can be increased by inducing selective radiation damage to tumor neovessels in a human pancreatic adenocarcinoma tumor model. To evaluate this, noninvasive MRI and whole body fluorescence imaging using short and long-circulating nanocarriers with different size distributions was employed. Experimental evidences demonstrate an increase in: i) quantitative tumor uptake, ii) tumor vascular permeability, and iii) intratumoral distribution of nanomedicines.

Results and Discussion

To improve drug delivery in *h*-PDAC, we sought to increase its tumor vascular permeability using targeted gold nanoparticles and radiation therapy (RT). Human pancreatic tumor models are characterized by low EPR (enhanced permeability and retention effect)– a pathophysiological feature that facilitates nanodrug accumulation and retention within the tumor[17,30–32]. By using tumor endothelial targeting gold nanoparticles and noninvasive external beam RT, tumor vascular disruption was induced. The transient alteration of tumor blood vessels effectively increase EPR, thus improving tumor-specific nanodrug accumulation (Fig. 1).

Physicochemical and *in vitro* characterization of gold nanoparticles. Heterobifunctional, PEG/cRGD modified gold nanoparticles (t-NP) were synthesized based on standard turkevich method[14,33]. With spherical morphology, t-NP had a core of 2–3 nm, a hydrodynamic size of 5–10 nm and zeta potential of + 7.55 mV (Fig. 2A,B) (Figure S1). Tumor endothelial targeting was attained by using cRGD - a standard vascular targeting ligand that docks to the transmembrane receptor proteins $\alpha_v\beta_3$ and $\alpha_v\beta_5$ present along the tumor vascular lumen[14,17,34]. Preliminary simulation studies have shown the impact of t-NP size on the emitted electron spectrum. A core size of 2–3 nm predicted the highest fluence of emitted electrons and subsequent photoelectric interactions (Fig. 2C). Further analysis of DNA double-strand breaks (DDSB) using Monte Carlo Damage Simulation (MCDS, v3.10 A) studies confirmed an increase in DDSB due to nanoparticle-radiation interactions (Table S1).

Radiation dose amplification is mediated by direct physical damage due to the emission of low-energy electrons that cause DDSB and indirect biological damage due to the release of OH^- (hydroxyl), H_2O_2 (peroxide) and O^{2-} (superoxide anions) (Fig. 2D)[35]. The radiation response of proliferating endothelial cells at 2 Gy and 4 Gy demonstrated increased cellular damage in combination with t-NP. More than two-fold increase in DDSB was quantitatively measured (Fig. 2E,F). Free radical generation from 15 min to 3 h post-RT at various t-NP concentrations showed that both 4 Gy and 10 Gy improved the free radical (primarily peroxide) mediated radiation damage in the t-NP + RT group compared to the 'no nanoparticle' control groups (Fig. 2G). High concentrations ($\geq$0. 8 mg/ml) of gold nanoparticles affected *in vitro* cell proliferation and induced toxicity and cell morphological changes in endothelial cells (Figure S2)[14,36]. Direct clonogenic response studies showed that t-NP induced radiosensitization with an SER (sensitivity enhancement ratio) of 1.35. Overall, t-NP + RT demonstrated significantly high cellular damage at 2 Gy ($P = 0.017$), 4 Gy ($P = 0.008$), 6 Gy ($P = 0.006$), and 8 Gy ($P = 0.0112$) compared to its RT-only treatment group (Fig. 2H).

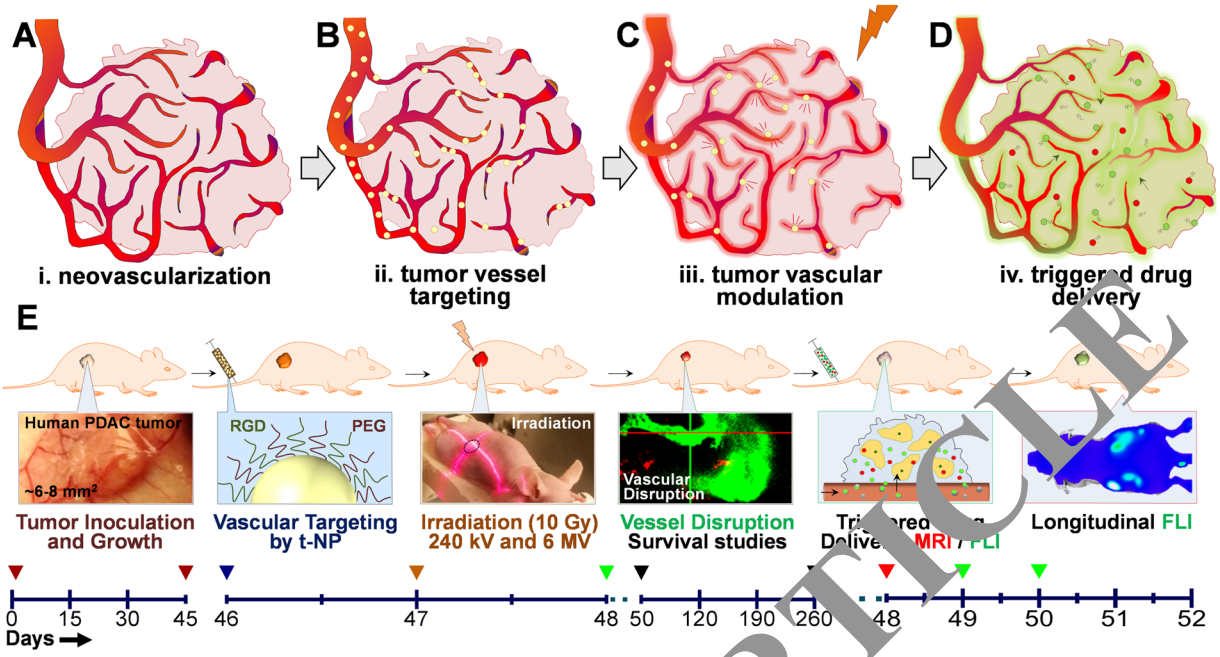

Figure 1. Concept and study design. A schematic depiction of r...-induced tumor vascular modulation to trigger and enhance tumor-specific drug delivery in a *h*-PDAC tumor model. (**A**–**D**) Angiogenic tumor blood vessels overexpressing $\alpha_v\beta_3$, $\alpha_v\beta_5$ integrin receptors a... the tumor neoendothelium were targeted using RGD-conjugated gold nanoparticles (shown in yellow). Upo... to (preclinical or clinical) radiation therapy, gold nanoparticles were activated to induce a physical v...cular damage. This selective vascular damage is explored to trigger and enhance drug delivery of *i.v.*-ad...inistered polymeric nanomedicines. Short-circulating MR-sensitive nanocarrier (red) and lon...-circ...ing fluorescence-sensitive nanocarrier (green) with different size dimensions were tested for enhan... paylo... delivery. (**E**) Timeline chart (in days) elaborates various experimental procedures that has...en im...mented. Following tumor inoculation and growth from day 0–45, the study was carried out in three stag... Phase I: Inducing selective radiation damage to *h*-PDAC tumor endothelium (day 46–48); Phas... imagi...g tumor vascular modulation and assessing the survival benefits (day 50–260); Phase III: Triggering ...mor-specific payload delivery of Gad-NC and FL-NC – two representative model nanodrugs used ... image-gu...ed drug delivery studies (day 48–52). Overall, this study involves the use of targeted (t-NP) and non...geted (NP) gold nanoparticles; preclinical (240 KV) and clinical (6 MV) radiation treatments; T_1-weighted, DCE-MR and whole-body fluorescence imaging studies using (Gad-NC and FL-NC respectively) a...ministered at stipulated time-points. For all the survival, treatment, and imaging studies, a tumor size of ≥ ...cm was considered as a terminal end-point.

The in...bition of fully formed angiogenic vessel formation during RT was tested out using the endothelial tube fo...ation assay or angiogenesis assay. Fluorescence-labeled primary human endothelial cells formed tube-like str...tures over a period of 4 h under specific cell culture conditions (see Materials and Methods). Combined NP + RT treatment damaged the vessel structures and resulted in endothelial cell damage, whereas the RT-only, t-... only, non-targeted NP + RT and other control treatments did not have any noticeable effect on endothelial tube formation (Figure S3).

Biodistribution and tumor localization studies. Following *i.v.*-administration of t-NP in *h*-PDAC mouse tumor models, the accumulation in tumor and peripheral organs were measured using ICP-MS. The mean tumor accumulation reached its maximum (~2.1% ID) at 24 h post-administration (Fig. 3A). Total area under the curve (AUC) calculated from tumor accumulation kinetics measured 1362 ± 13.68% ID/g.h. (Figure S4). t-NP distribution steadily declined at 24 h in other vital organs such as the heart, lung, spleen, liver and kidney. In heart and kidneys, t-NP concentrations reduced to 0.13% ID/g and 1.7% ID/g, respectively. Non-specific uptake in liver contributed to 6.2% ID/g accumulation. Overall, the tumor: organ ratio was higher at 24 h. Other reported studies have shown that gold nanoparticles of ≤10 nm that tend to accumulate in the liver is cleared *via* hepatobiliary pathways over an extended period of several months[24,37].

t-NP accumulation in the tumor blood vessels was confirmed by LIBS (Laser-induced breakdown spectroscopy imaging) imaging – a technique that accurately detects endogenous metals and correlates with real-time hyperspectral data. LIBS captured gold (*Au*) signals from the *in vivo* tumor specimens collected at 1 h and 24 h post-administration (Fig. 3B). A cross-examination of tumor slices show heterogeneous distribution of t-NP in the tumor periphery as well as in the core. In agreement with the biodistribution data, maximum t-NP accumulation was observed at 24 h. A robust correlation was observed between the *Au* (yellow) from t-NP and *Fe* (red) from stagnated tumor blood vessels (Fig. 3C). *Au - Fe* correlation ratio was measured to be 0.65, providing some evidence for the co-localization of nanoparticles with tumor blood vessels (Figure S5). A spectral peak at 268 nm

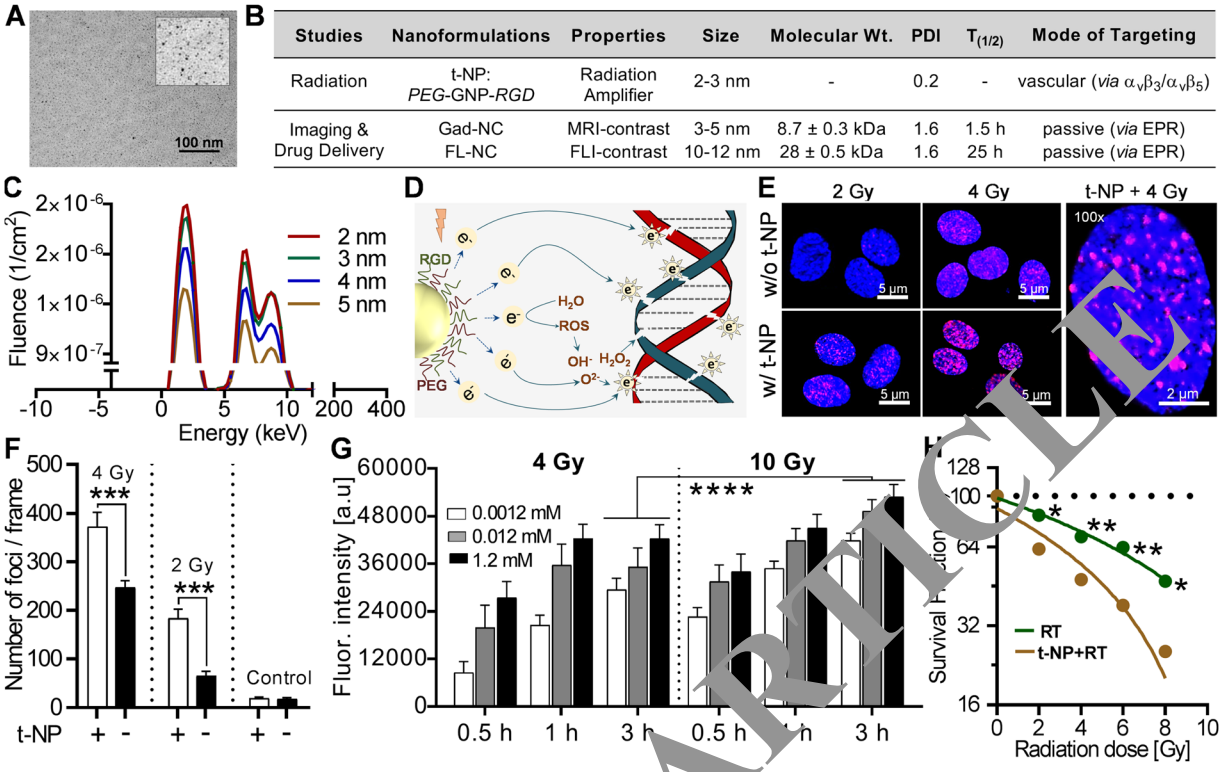

Studies	Nanoformulations	Properties	Size	Molecular Wt.	PDI	$T_{(1/2)}$	Mode of Targeting
Radiation	t-NP: *PEG*-GNP-*RGD*	Radiation Amplifier	2-3 nm	-	0.2	-	vascular (*via* $\alpha_v\beta_3/\alpha_v\beta_5$)
Imaging & Drug Delivery	Gad-NC FL-NC	MRI-contrast FLI-contrast	3-5 nm 10-12 nm	8.7 ± 0.3 kDa 28 ± 0.5 kDa	1.6 1.6	1.5 h 25 h	passive (*via* EPR) passive (*via* EPR)

Figure 2. Physicochemical characterization and *in vitro* radiation damage amplification. (**A**) High-resolution TEM imaging shows ultrasmall gold nanoparticles with a core size of 2–3 nm (cf. inset) bi-functionalized with *Arg-Gly-Asp* (RGD) and PEG (polyethylene glycol). (**B**) Nanoformulations used in this study is summarized in the table. Endothelial-targeted gold nanoparticle (t-NP) were employed to mediate a radiation-specific tumor vascular modulation. MR and fluorescence contrast polymeric nanocarriers (Gad-NC and FL-NC) with diverse physicochemical properties were used for enhanced image-guided drug delivery studies. (**C**) Preliminary simulation tests show a linear relationship between the ejection of low energy photoelectrons from gold nanoparticles at its respective sizes. NP, with a core size of 2–3 nm is predicted to generate superior radiation amplification due to the reduced self-absorption of Auger electrons. (**D**) Schematic illustration of physical and biological radiation interactions that eventually leads to DNA double-strand breaks (DDSB). Low energy electrons generated due to the radiosensitization of t-NP induce direct DDSB and the simultaneous generation of free radical's invoke an indirect DNA damage. (**E**,**F**) DNA damage studies following radiation and (+/−) t-NP treatment show distinct differences (~two-fold) in DDSB in proliferating human endothelial cells. Further quantification of damaged foci confirmed significant differences between nanoparticle-treated *versus* non-treated groups under different irradiation conditions. **G**. Free radical assays (primarily for peroxides) at three different t-NP concentrations (0.0012, 0.12, and 1.2 mM) demonstrate dose-dependent changes in the free-radical damage at different time point's post-RT in human endothelial cells. Fluorescence intensity changes corresponds to the number of reactive oxygen species detected. The data were normalized to the non-treated control 0 Gy and without t-NP. (**H**) Linear, quadratic regression plots of endothelial cell survival demonstrated significant differences at 2 Gy ($P = 0.018$), 4 Gy ($P = 0.009$), 6 Gy ($P = 0.006$) and 8 Gy ($P = 0.011$) in t-NP + RT *vs.* RT-only treatment. All results were normalized to its respective treated and non-treated controls. Error bars are smaller than the dotted plots.

further confirmed the presence of *Au* (Fig. 3D). Histological prussian staining of tumor samples collected at 24 h and microscopy imaging provided additional evidence for the presence of *Au* along the *h*-PDAC endothelial walls (Figure S6).

Tumor vascular modulation and survival studies. Biodistribution and microscopy data confirmed 24 h as ideal time-point for RT due to the high tumor to organ ratio and the substantial t-NP localization along the tumor neoendothelium. Clinical-RT (6 MV) was applied to the tumor with the body shielded by primary tungsten collimators. Radiation dose distribution calculations confirmed that ≥99% of the tumor region received a minimum dose of 10 Gy, while sparing the normal tissues (Fig. 4A). A long-term survival rate of 80% was observed in the t-NP + RT group, with all surviving mice exhibiting 100% tumor regression and no signs of collateral toxicity (Fig. 4B). Repeating this study with preclinical-RT (220 kVp) and t-NP also demonstrated a significant antitumor effect (Figure S7). Further histological evidences confirmed tumor vascular disruption following t-NP + RT treatment using clinical-RT (6 MV, 10 Gy) (Fig. 4C). Morphological changes in the tumor neovasculature, loss of endothelial integrity, and specific blood vessel rupture were evident in t-NP + RT cohorts at 24 h post-RT. However, the control groups showed intact and functional tumor blood vessels with no morphological changes. Red blood cells (RBC) underwent apoptotic changes

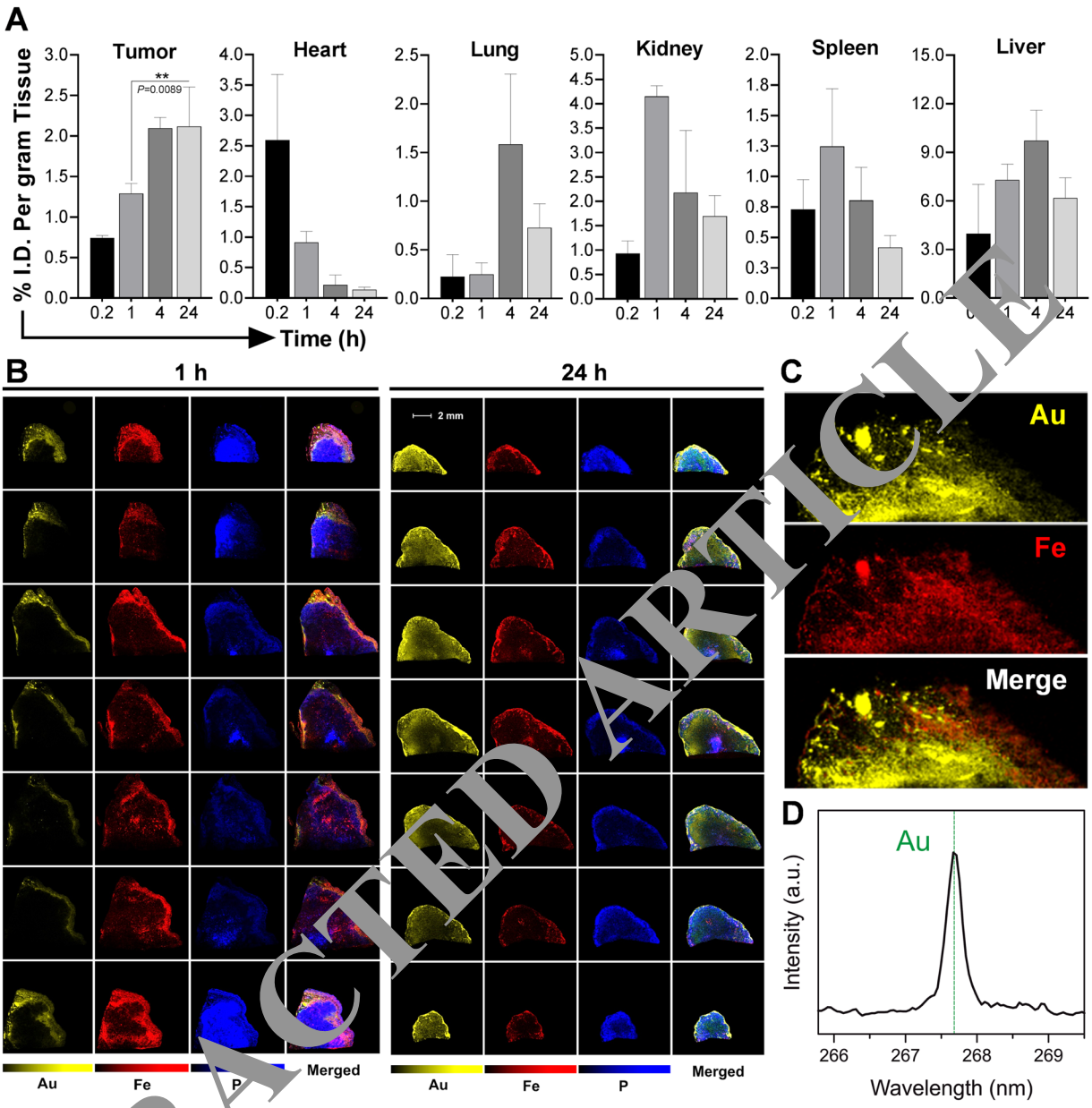

Fig. 3. Biodistribution and tumor localization studies. (**A**) Quantitative biodistribution of t-NP in tumor and various organs were measured by ICP-MS following its *i.v.*-administration in Capan1 tumor-bearing mice ($n = 5$). At 24 h, maximum tumor accumulation was noticed with comparably less accumulation in other vital organs. (**B**) Laser-induced breakdown spectroscopy imaging was performed to qualitatively estimate the intratumoral distribution of t-NP. The symbols correspond to, *Au* – Gold (indicative of t-NP), *Fe* – Iron (a surrogate marker for tumor blood vessels) and *P* – Phosphorus. The presence of *Au* from t-NP and *Fe* from the heme of RBCs conveyed specific imaging signals. A complete tumor analysis from tumor periphery to the core demonstrate heterogeneous distribution of nanoparticles. 24 h tumor samples exhibit maximum t-NP distribution, and *Au* was observed in close proximity to the tumor blood vessel signal (red). (**C**) High-magnification LIBS imaging revealed substantial overlap of *Au* and *Fe* in a 24 h tumor sample. (**D**) Real-time spectral analysis demonstrated a corresponding peak for *Au* (yellow) at 267.595 nm and confirmed its intratumoral accumulation in an *h*-PDAC tumor model.

in t-NP + RT treatment (Fig. 4C). Histological evidences confirmed the depletion of supporting smooth muscle actins (α-SMA) (Fig. 4C). Radiation-specific gamma-H2AX staining indicated massive DNA double strand breaks (brown nuclei) under t-NP + RT treatment conditions (Fig. 4C). Functional perfusion studies using FITC-dextran exhibited considerable loss of vessel integrity, leading to FITC diffusion (Fig. 4C). However, the blood vessels in the control groups remained largely intact, non-permeable, and functional with steady perfusion of FITC-Dextran. No toxicity was observed in other vital organs following t-NP + RT treatment (Figure S8). Further changes in tumor vascular modulation and its downstream physiological changes were evaluated using FLI and MRI.

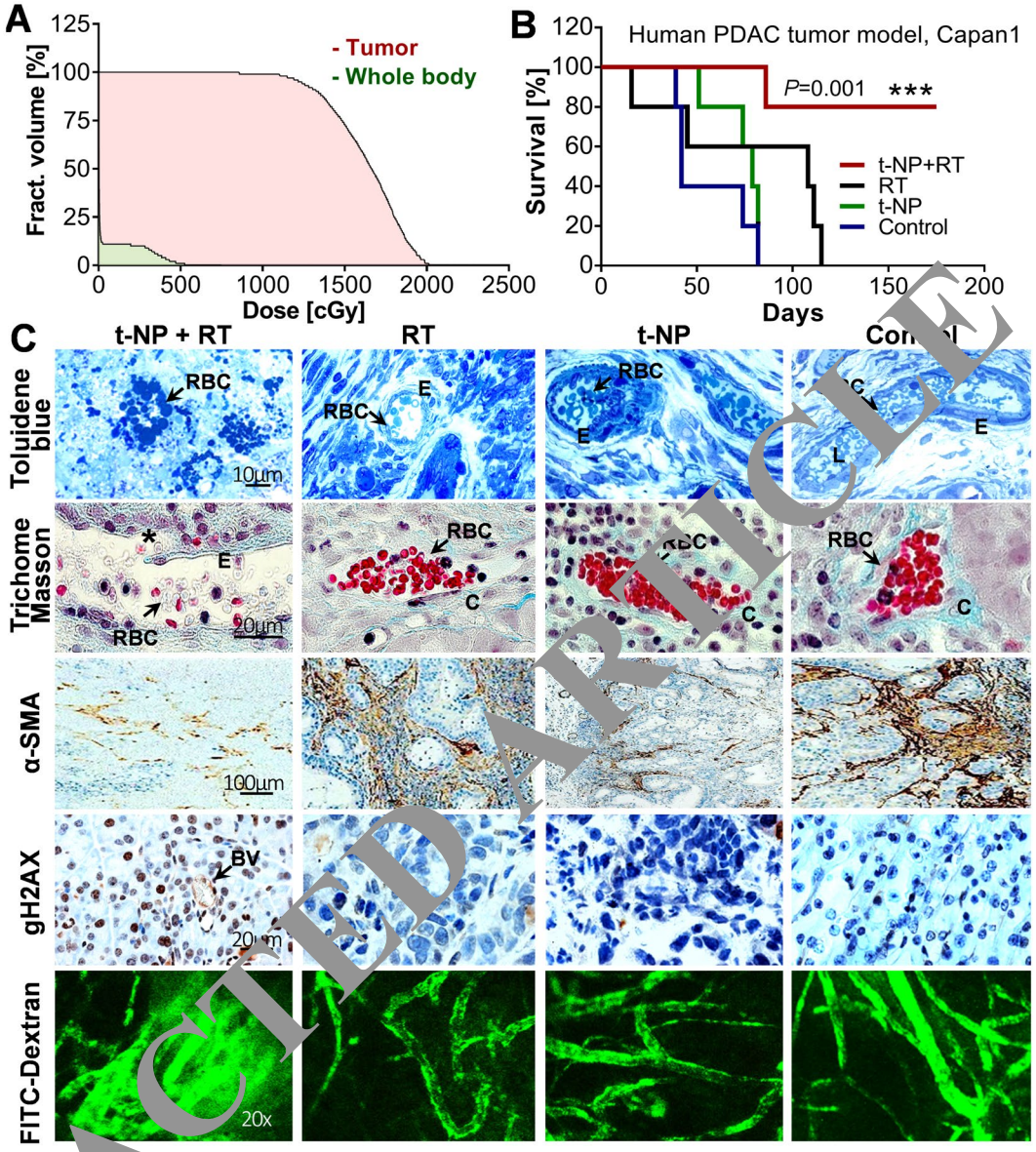

Figure 4. Tumor vascular modulation and survival studies. Tumor-selective radiation damage elicited changes in vessel morphology and survival in *h*-PDAC. t-NP was administered intravenously at a dose of 1.2 mg/g and irradiations were carried out at 24 h post-administration. (**A**) A dose-volume histogram measured tumor dose delivery in comparison to the rest of the body in a clinical beam-RT set-up (6 MV, 10 Gy). Dose measurements recorded >99% of radiation coverage to the tumor region at a dose of 10 Gy. (**B**) Kaplan-Meier plot depicting survival studies using clinical beam RT (6 MV, 10 Gy) demonstrate an improved therapeutic benefit with t-NP + RT treatment. Log-rank (Mantel-Cox) tests were used for statistical analysis. **C**. Histological and perfusion evidences confirmed vascular modulation at 24 h post-treatment. Toluidine blue and trichome Masson stainings confirmed the disruption of tumor neovessels during combined nanoparticle and radiation therapy. Selective rupture (asterisks) resulting in non-functional and apoptotic RBC's (arrows) and vascular instability was observed. However, functionally-viable and collagen-sheathed vessels were observed in other control samples. DNA damage studies using gamma h2ax confirmed radiation-specific damage in tumor cells and tumor blood vessels. Brown color indicates DNA damage. Smooth muscle actins (α-SMA; brown) that support the tumor endothelium was largely compromised during radiation and nanoparticle-induced tumor vascular modulation. Functional (or perfusion) changes assessed by the FITC-dextran infusion (70 kDa) show extensive leakage (or permeation of FITC) in selective, treated vessels in t-NP + RT groups. In all other treatment conditions, tumor blood vessels remained intact, distinctly labeled, with no indicated signs of passive leakage into the tumor interstitial spaces. RBC: red blood cells; E: endothelium; L: lumen; C: collagen; BV: blood vessel.

Enhancing tumor-specific drug delivery. By modulating the tumor vascular barrier, we anticipate enhancement in tumor-specific nanodrug delivery to *h*-PDAC tumors. To evaluate this, we employed two prototypical nanodrug carriers - each with different size, circulation, and imaging kinetics: i) a short-circulating MR-sensitive

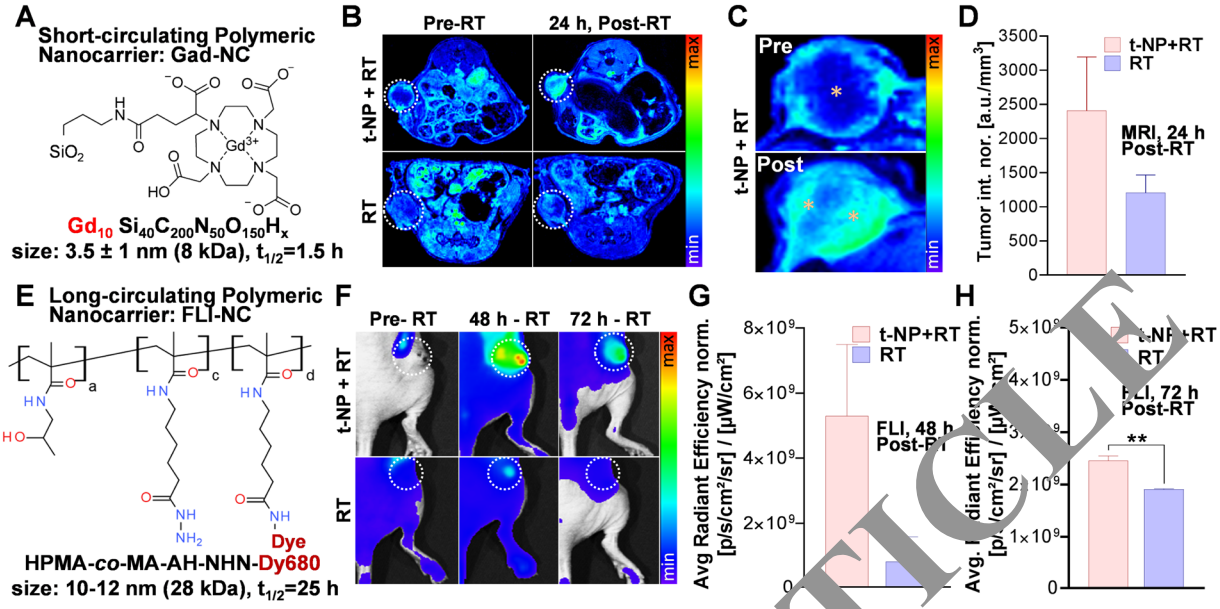

Figure 5. Enhanced image-guided drug delivery in human pancreatic tumor model (*h*-PDAC). To trigger and enhance drug delivery post-tumor vascular modulation using t-NP and RT, two nanocarriers with short- and long circulating properties were used. (**A**) Gadolinium-based contrast formulation (Gad-NC) was used to perform tumor uptake studies pre and post-tumor vascular disruption. T_1-weighted MR imaging demonstrated an enhanced Gad-NC uptake in t-NP + RT group compared to the RT-only group. (**C**,**D**) Magnified image show intratumoral distribution of Gad-NC. Heterogenous distribution in the core and peritumoral regions (yellow stars) were observed. Upon further quantification, a two-fold difference between the t-NP treated *vs*. non-treated cohorts was noted. (**E**,**F**) A long-circulating polymeric nanocarrier of HPMA coupled to a nearinfrared fluorescent dye (FL-NC) was administered to mice bearing capan1 pancreatic tumor, and fluorescence imaging were performed. A longitudinal accumulation of FL-NC in higher amounts was noticed in the t-NP + RT-treated tumors, both at 48 h and 72 h. (**G**,**H**) Further quantification of fluorescence showed a ≥ two-fold increase in the accumulation of FL-NC. All values were normalized to its respective standards.

gadolinium nanocarrier (Gad-NC) and ii) a long-circulating fluorescence-sensitive HPMA nanocarrier (FL-NC) (Fig. 5A). Due to its small size (1–5 nm) and molecular weight (8.7 kDa), Gad-NC shows rapid systemic circulation ($t_{1/2}$ = 1.5 h) and renal clearance[38–40]. Maximum tumor uptake of Gad-NC was obtained at 15–30 mins after intravenous administration[41,42]. Under different treatment conditions, T_1-weighted MRI of Gad-NC demonstrated an overall increased tumor accumulation in the t-NP + RT group at 24 h post-RT (Fig. 5B). Intratumoral uptake analysis of the tumor MRI images showed prominent distributions of Gad-NC in the periphery and core of the tumor, as opposed to the RT-only group with prominent peripheral contrasts (Fig. 5C). MRI-based quantifications confirmed two-fold difference in the accumulation of Gad-NC in the t-NP + RT treatment group *vs*. RT-only treatment group (Fig. 5D). To further investigate the influence of size and the dynamics of tumor accumulation for an extended time post-RT, an HPMA-based fluorescent nanocarrier (FL-NC) was employed (Fig. 5E). HPMA-based drug delivery systems are used for EPR-mediated drug targeting due to their prolonged circulation half-life, biocompatibility, and non-immunogenicity[17,39]. Due to its hydrophilicity, HPMA-based polymeric carriers are characterized by predictable kinetic behavior and are widely used for image-guided drug delivery applications[40,43,44]. Following *i.v*-administration of FL-NC, fuorescence imaging measured more than two-fold increase in its accumulation in *h*-PDAC at 48 h and 72 h in the t-NP + RT group compared to the RT-only group (Fig. 5F-H). *Ex vivo* tumor samples collected at 72 h qualitatively and quantitiatively confirmed this increase in FL-NC accumulation in the t-NP + RT group compared to other treated and non-treated controls (Figure S9).

Assessment of tumor blood vessel functionality. Alteration in tumor blood vessels following t-NP + RT treatment can cause measurable changes in permeability (K_{trans}), extravascular back-flux (K_{ep}), and extravascular extracellular volume fraction (V_e) (Fig. 6A). DCE-MRI studies at 24 h post-RT demonstrated an increase in tumor vascular permeability (K_{trans}) for the t-NP + RT group compared to the RT-only group (Fig. 6B). K_{ep}– a parameter that best depicts changes in the tumor or interstitial retention of Gad-NC indicated a low extravascular backflux into the plasma for the t-NP + RT group. It complied with the permeability changes (described above) and justified nanodrug accumulation in the 'vascular modulated' group. Further quantitative measurements of V_e – an extracellular extravascular volume fraction parameter – provided insight into the intratumoral uptake of Gad-NC, which was higher for t-NP + RT *vs*. RT-only. This analysis of various DCE-MRI parameters revealed a distinctive difference in K_{trans}, K_{ep}, and V_e among the t-NP + RT and RT-only tumors (Fig. 6C–E). Acute changes in the tumor vascular permeability, measured from the tumor periphery to the core by segmenting the whole tumor into five segmented regions, demonstrated an overall increase in vascular

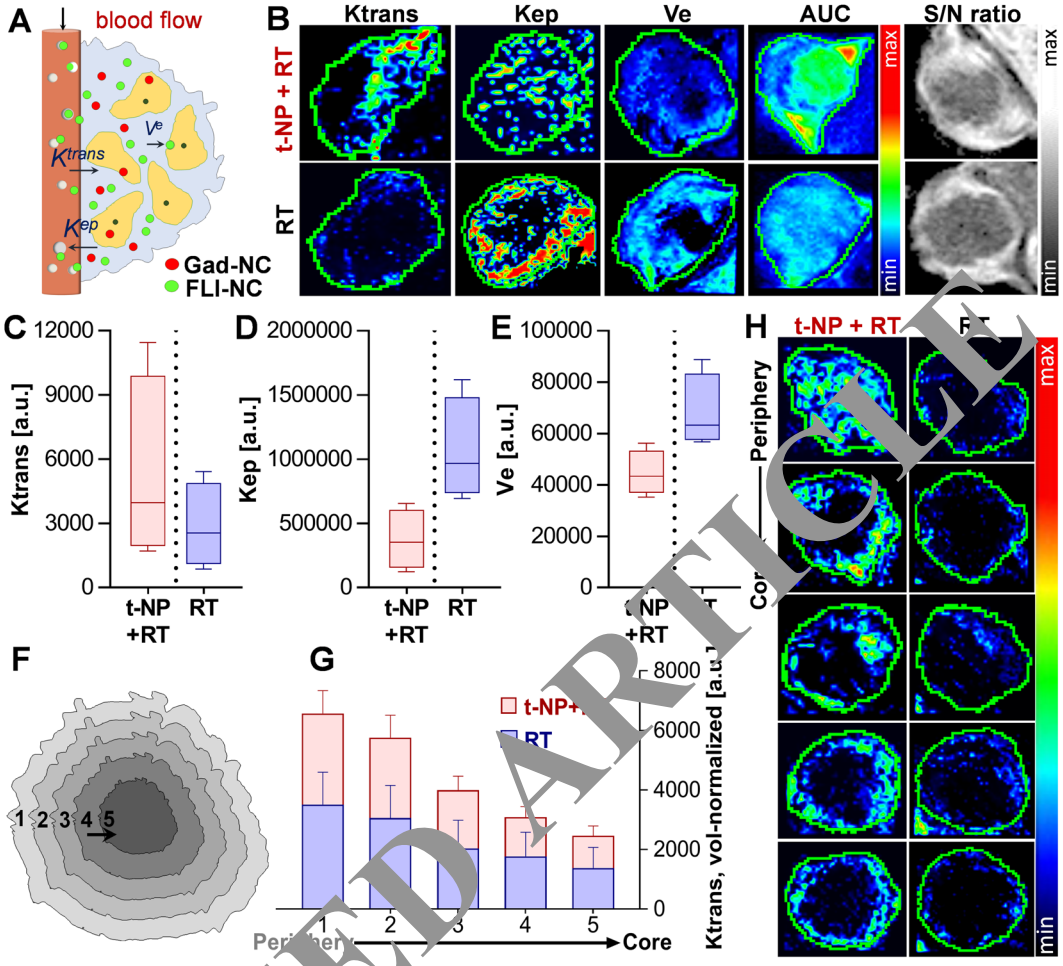

Figure 6. Measuring functional changes during tumor vascular modulation. (**A**,**B**) Dynamic changes in the tumor vascular parameters K_{trans} (transendothelial permeability), K_{ep} (extravascular back-flux), and V_e (extravascular extracellular volume fraction) were measured using DCE-MRI after *i.v.*-administration of Gad-NC to *h*-PDAC tumor-bearing mice. DCE-MRI studies displayed a qualitative increase in the tumor vascular permeability (K_{trans}) following tumor vascular modulation, and associated decrease in K_{ep} (back-flux into the plasma) and V_e (the extravascular extracellular volume fraction) parameters. (**C**–**E**) Further changes induced by t-NP + RT treatment was measured by an increase in K_{trans} (permeability) and a concomitant decrease in K_{ep} (retention) and V_e (uptake) – prototypical responses of an anti-vascular treatment. Discontinuous lines relate to the 'tumor vascular modulation' by t-NP + RT treatment *vs*. 'no modulation' in RT-only treatment. (**F**,**G**) Intratumoral changes in tumor vascular permeability from its periphery to the core (in the 3D tumor) was measured. The corresponding K_{trans} plots show a distinct increase in endothelial permeability from the tumor periphery to the core in vessel-modulated t-NP + RT cohorts, compared to the RT-only cohorts. (**H**) Two-dimensional tumor slices were analyzed, and K_{trans} changes were further qualitatively confirmed.

permeability (K_{trans}) from the core to the periphery (Movie S1, S2). In all segmented tumor slices, the vascular permeability was higher in t-NP + RT treated tumors (Fig. 6F–H).

Conclusion

This study aims to improve drug delivery by invoking changes in tumor neovessels using combined nanoparticle and external beam radiation therapy. Alterations in tumor blood vessels using radiation and nanoparticle combined therapy led to an increased tumor payload delivery. Tested using two prototypical nanodrugs, further physiological changes caused by tumor vascular modulation was measured using noninvasive MRI and fluorescence imaging. Experimental evidences demonstrate a substantial improvement (almost double) in image-guided drug delivery post tumor vascular modulation. Vascular parameters, measured by DCE-MRI confirmed these results. Our findings propose a new way to overcome the tumor vascular barrier and improve targeted drug delivery.

Experimental Section

Monte Carlo simulation studies. Monte Carlo simulations were employed to study the radiobiological DNA damage enhancement of gold nanoparticles. We have used two-step simulations for calculating the damage in the DNA. In the first step, FLUKA Monte Carlo code was used to calculate the electron energy spectra produced from 220 kVp X-ray photon interaction with cell media and gold nanoparticles. The 220 kVp X-ray photon

spectrum was estimated with a gaussian distribution with an average energy of 140 kV and FWHM of 77.7 kV. The media in the cell dish was assumed to be water with 3 mm thickness. For the gold nanoparticle simulations, 2 to 5 nm diameter spherical nanoparticles were simulated. In step 2, MCDS software (v3.10 A) was used to calculate the damage spectra that are produced in a cell as a result of the emitted electrons. The MCDS software considers direct and indirect damage to DNA induced by electrons and charged particles and computes base lesion (BL), single strand break (SSB), double-strand break (DSB) frequencies.

Synthesis and characterization of nanoformulations. i) Gold nanoparticles for tumor vascular targeting

Gold nanoparticles were prepared using previously reported protocols[14,33]. Briefly, colloidal gold was prepared by reduction of gold salt (chloroauric acid) in the presence of a stabilizing/reducing agent, tetrakis (hydroxymethyl) phosphonium chloride (THPC). THPC-stabilized gold nanoparticles were PEGylated by ligand exchange process using a mixture of thiolated (-SH) PEG derivatives (MW: 2 kDa). PEG-stabilized gold nanoparticles were covalently conjugated to *Arg-Gly-Asp* (RGD) and a near-infrared dye, AF647 by reacting with the carboxylic (-COOH) and amine ($-NH_2$) pendant functional groups. The nanoparticles (t-NP) were further subjected to membrane-dialysis by using a 12–14 kDa cellulose membrane against purified double-distilled water, to remove traces of unreacted EDCI or other hydrolyzed products along with unreacted RGD molecules. The final solution consisted of purified t-NP, which were further characterized for particle size (DLS), surface morphology (TEM) and the absorption/ excitation values.

ii) Gadolinium nanocarrier (MR-NC): Model nano-drug and MR contrast agent.

Gad-NP were synthesized and purified in compliance with GMP standards at Nano-H (Lyon, France)[45,46]. Gad-NP is composed of an inorganic matrix of polysiloxane surrounded by covalently bound DOTAGA (Gd) (1,4,7,10-tetra-azacyclododecane-1-glutaric anhydride - 4,7,10-triacetic acid) - Gd^{3+}).

iii) HPMA (N-(2-hydroxypropyl) methacrylamide) based polymeric nanocarrier (FL-NC): Model nanodrug of fluorescence imaging agent.

The HPMA based copolymer (pHPMA) constructs conjugated with a near-infrared labeled fluorescent dye (FL-NC) were used for fluorescence-based studies. The synthesis was carried out in two steps where the fluorescent dye Dy-676 as a model drug was modified to form an oxo derivative and later chemically conjugated via pH-sensitive hydrazone bond to the pHPMA.

a. **A derivative of Dy-676** (or COP-Dy-676): COP-Dy676 was prepared by earlier reported protocols[43]. Briefly, 5-cyclohexyl-5-oxopentanoic acid (COP) reacted with 2-thiazolidine-2-thione in the presence of *N,N'*-dicyclohexyl carbodiimide (DCC) in tetrahydrofuran solution at 0 °C. The reaction was catalyzed with 4-(dimethylamino) pyridine to yield 5-cyclohexyl-5-(2-thioxothiazolidin-3-yl)pentane-1,5-dione (COP-TT). COP-TT (0.6 mg, 1.98 µmol) was then dissolved in dimethylacetamide (0.12 mL) with diisopropylethylamine (0.3 µL, 1.98 µmol) and Dy-676-amine (1.64 mg, 1.98 µmol). The product was isolated by precipitation with diethyl ether followed by filtration to yield 1.9 mg (1.88 µmol, 95%) of COP-Dy676.

- N-(2-hydroxypropyl) methacrylamide (HPMA) was synthesized as described previously[47]. M.p. 69–70 °C; purity >99.8% (HPLC), elemental analysis: calculated: C-58.72%, H-9.15%, N-9.78%; found: C-58.98%, H-9.18%, N-9.82%.
- 6-methacrylamidohexanohydrazide (Ma-ah-$NHNH_2$) was synthesized based on previously reported protocols[48]. M.p. 79–81 °C; elemental analysis: calculated: C-56.32%, H-8.98%, N-19.70%; found: C-56.49%, H-8.63%, N-19.89%.
- The final polymer carrier containing free hydrazide groups - a random copolymer of HPMA with Ma-ah-$NHNH_2$-(pHMA) was prepared by radical copolymerization in methanol (AIBN, 0.8 wt. %; monomer concentration 18 wt.%; HPMA: Ma-ah-$NHNH_2$ molar ratio = 93:7; 60 °C; 17 h) as previously reported[43].

b. **Conjugation of pHPMA with COP-676, FL-NC preparation:** pHPMA copolymer containing 7 mol% of hydrazide groups (90 mg) was dissolved in 0.2 mL of methanol with COP-676 (1.84 mg) and 40 µL of acetic acid at 25 °C. Next day, the reaction mixture was diluted with 0.5 mL of 0.01 M phosphate buffer pH 7.4 with 0.14 M NaCl (PBS) and chromatographed on Sephadex LH 20 using methanol as a mobile phase. The polymer fraction was concentrated under reduced pressure and precipitated into diethyl ether to yield 70 mg of blue powder. The content of Dy-676 in the conjugate 1.4 wt.% were determined spectrophotometrically.

Characterization of nanoformulations. Lyophilized nanoparticles were dispersed in PBS (7.4) for one hour at room temperature. Hydrodynamic size and zeta potential measurements were carried out with a Zetasizer Nanos DLS (Malvern Instruments, UK) at further diluted concentrations. The molecular weights and polydispersity of the copolymers were determined by using size exclusion chromatography (Shimadzu HPLC system, Shimadzu) equipped with a refractive index, UV, and multiangle static light scattering (Wyatt Technology Corporation, CA) detectors using a TSK 3000 SWXL column (Tosoh Bioscience, Japan) using 80% methanol, 20% 0.3 M acetate buffer (pH 6.5) at a flow rate of 0.5 mL/min. The calculation of molecular weights from the light-scattering intensity was based on the known injected mass, assuming 100% mass recovery.

Cell culture studies. Human pancreatic adenocarcinoma cell line Capan-1 (ATCC HTB-79) were cultured in Iscove's modified DMEM (GIBCO, USA), supplemented with 20% fetal bovine serum (Invitrogen, USA) and 1% Pen/strep (10,000 U/mL penicillin; 10,000 µg/mL streptomycin, Invitrogen, USA) respectively. The culture was maintained at 37 °C and 5% CO_2 under an optimal relative humidity of 90%.

Free radical assay. Human umbilical vein endothelial (HUVEC, ATCC CRL-1730) cells were seeded in 96-well plates (10,000 cells/well) and cultured for 24 h. The cells were then incubated with different concentrations of t-NP for 24 h and washed with PBS to remove nanoparticles that were not internalized by the cells. Afterward, cells were incubated with 10 μM dihydrodamine 123 (DHR123) for 3 h. Before the irradiation, cells were washed with PBS to remove the excess of DHR. Irradiations were performed with a single fraction of 4 Gy (220 kVp) with and without t-GNP. The fluorescence signal was measured from 1 to 3 h post-irradiation using a plate reader (POLARstar omega, BMG LABTECH, Germany) with an excitation wavelength of 480 nm and an emission wavelength of 520 nm.

MTS cell viability assay. HUVEC cells (10,000 cells/well) were seeded in 96-well plates and grown for 24 h. The cells were then incubated with different concentrations of nanoparticles diluted in cell culture media for 1 and 24 h. 20 μL of MTS solution (CellTiter 96, Promega) was added to each well and incubated for 3 h at 37°C, to allow the formation of formazan crystals. These crystals were then dissolved, and the absorbance was measured at 490 nm (POLARstar omega, BMG LABTECH, Germany).

DNA damage assay. One hour after irradiation, cells were fixed to study the damage on HUVEC cells with and without the presence of gold nanoparticles (t-NP). Histological stainings were performed. Briefly, cells were blocked and permeabilized with 1% BSA, 10% FBS, and 0.3% Triton X-100 for 1 h at room temperature. For γ-H2AX staining, cells were incubated with primary anti-body (Merck Millipore) and anti-mouse secondary antibody (AlexaFluor 488, Molecular Probes, USA). Immediately after, the coverslips were mounted with DAPI and Fluoromount-G (Southern Biotech, USA). Images were analyzed by a confocal laser scanning microscope Olympus FV3000.

Clonogenic assay. HUVEC were incubated with 0.6 mg/mL of t-NP for 1 h in a 10-cm dishes with a seeding density of 300 cells per well. Irradiations were performed with a 220 kVp beam for 2, 4, 6, and 8 Gy at a dose rate of 4 Gy per minute. The cells were further allowed to grow for 7 days before staining with 1% crystal violet in 10% ethanol dye solution was carried out. The treatment effect of t-NP was quantified by the calculating dose enhancement factor (DEF) using Matlab (v. R2013b).

Angiogenesis tube formation assay. Human umbilical vein endothelial cells were treated with calcein AM (Life Technology) for 30 minutes at 37°C with 5% CO_2 to acquire GFP-like positive staining. The cells suspended in the cell culture medium were centrifuged at 1.5 x10^3 RPM twice to wash out the excess calcein in the medium. The cells (15x10^3 cells/well) were then mixed with VEGF + ve HUVEC cell culture medium (Lonza, Switzerland), and further plated on a growth factor reduced basement membrane matrix (Corning, NY) in 96 well plates[49]. At 37 °C and 5% CO_2, the cells were incubated for almost 4 hours for angiogenic tube formation. The tubes were treated with targeted and non-targeted gold nanoparticles (t-NP, NP) and radiation treatment (2 Gy) was applied at 8 h using the Small Animal Radiation Research Platform (SARRP, Xtrahl, Inc. Suwanee, GA). Excess nanoparticles that were not taken up the endothelial cells were removed by washing (3x) with the cell culture medium. Microscopic time-lapse imaging (Zoe fluorescence cell imager, BioRad, Hercules, CA) was carried out at 0, 1, 4, and 12 h and images were captured using a 5x objective at 100x magnification and further analyzed using ImageJ software. All five treatment conditions were performed in triplicates.

Inductively-coupled plasma mass spectrometry (ICP-MS) based biodistribution studies. Samples were digested using a combination of hydrochloric acid (HCl), nitric acid (HNO_3) and hydrogen peroxide (H_2O_2). All reagents used in the digestions were traced-element pure – either distilled in-house (HCl and HNO_3) or purchased at Optima grade (H_2O_2). Samples were initially digested in 3 ml HCl and 1 ml HNO_3 on a hotplate at 100 °C overnight. Samples were removed from the hotplate, and 1 ml of H_2O_2 was added drop-by-drop (the reaction with organic matter can be quite vigorous), and then they were placed back on the hotplate at 100 °C overnight. The samples were dried to near-dryness, and 2.5 ml of HCl was added, followed by another overnight heating on the hotplate, followed by the addition of 1 ml of H_2O_2. This step was repeated once. Finally, 0.3 ml of HCl and 0.25 ml of H_2O_2 was added and diluted to a final volume of 10 ml with Milli-Q water (to make 3% HCl). Heart, bladder, spleen and tumor samples were further diluted a 100x with 3% HCl; whereas kidney, lung and liver samples required a 200x further diluted with 3% HCl to prepare for ICP-MS analysis. Gold concentrations were measured on a VG Plasma Quad Excell ICP-MS. The samples were introduced to the instrument in solution form, through a Meinhard-C concentric nebulizer at a flow rate of ~1 mL/min. Since gold is mono-isotopic, measurements were made on ^{197}Au. Instrumental drift was monitored and corrected for by analyzing a 1 ng/g Au standard at various times throughout the run (every 5 analysis items). A calibration curve was generated by analyzing Au standards of varying concentration (from 0.01 ng/g to 10 ng/g) interspersed throughout the analytical run, and this curve had r^2 of 0.9999. Final *Au* concentrations were determined by comparing the signal intensity of samples from the calibration curve.

Laser-Induced Breakdown Spectroscopy (LIBS) imaging. LIBS imaging was performed based on previously reported protocols[41]. Briefly, epoxy-embedded tumor samples harvested 1 h and 24 h after t-NP administration were used for LIBS imaging. Up to 7 tumor slices, vertically spaced by about 1 mm, were analyzed for each of the studied samples. The instrumental setup included an optical microscope combined with a laser injection lineand a 3D motorized platform for sample positioning. We used Nd: YAG laser pulses of 1064 nm and 1 mJ, which were vertically focused onto the sample by a 15x magnification objective to produce the laser-induced plasma. The pulse duration was 5 ns, and the repetition rate was 10 Hz. The epoxy-embedded tumor sample

was translated along two axes to image, pixel by pixel, the region of interest. The signal was collected using a Czerny-Turner spectrometer and the final image resolution was 18 μm. The spectral range covered 250 to 330 nm to detect the following elements: *Au* (267.595 nm), *Fe* (302.064 nm) and *P* (253.560 nm).

Preclinical radiation therapy. Mice bearing Capan 1 human pancreatic tumor xenograft (6–8 mm^2) were irradiated using the Small Animal Radiation Research Platform (SARRP, Xtrahl, Inc. Suwanee, GA). Animals were anesthetized using 1–3% v/v isoflurane during both radiation and imaging procedures. Cone beam computed tomography (CBCT) imaging was performed on each mouse for setup and dose calculation (65 kVp, 1.5 mA). A single dose radiation of 10 Gy was administered using two different orthogonal beams at 0 and 90-degree angles with a 15 mm circular collimator (220 kVp, 13 mA). Four different treatment arms were included for both survival and drug delivery studies: + (t-NP)/ + RT; -(t-NP)/ + RT; + (t-NP)/-RT; -(t-NP)/-RT at $n = 5$ per group.

Clinical radiation therapy. Capan1 tumor-bearing mice were anesthetized following intraperitoneal administration of 0.1 mL/ 20 g mouse wt. of ketamine/ xylazine mixture. A 10-cm block of solid water (CIRS, Inc) was placed between the mouse and radiation source and an additional 2 cm of tissue equivalent clinical bolus material placed on top for backscatter. A clinical radiation treatment planning system (Eclipse v.11, Varian Medical Systems, CA) was used to calculate the radiation dose distribution in the tumor and the surrounding healthy organs. The AAA calculation algorithm for a 5.5 x 10 cm^2 field size, gantry at 180°, and surface-skin distance of 90 cm was applied in this study. Capan-1 tumor-bearing mice were injected with ~1.25 mg/g of t-NP *i.v.* and 24 h post-injection, radiation treatment at a dose of 10 Gy was performed. Four groups, + (t-NP) / + RT; -(t-NP) / + RT; + (t-NP) /-RT; -(t-NP) /-RT ($n = 5$), were used to characterize the effect of the t-NP as a tumor vascular modulating agent.

***In vivo* studies and animal tumor models.** Animal studies were approved by the DFCI Institutional Animal Care and Use Committee (IACUC, 14–032) and conducted in full compliance with the Association for the Assessment and Accreditation of Laboratory Animal Care, governmental and institutional regulations and principles outlined in the United States Public Health Service Guide. Immunocompromised CrTac: NCr-*Fox1nu* mice (Taconic Biosciences, Inc) were injected with 5×10^6 Capan 1 cancer cells subcutaneously in the right dorso-lateral flank. Tumors were allowed to reach a size of ~ $200\ mm^2$ before carrying out other *in vivo* experiments. All animals were conditionally inhalation-anesthetized (except for clinical-RT) during all operations.

Tumor vascular modulation and survival studies. Capan-1 tumor-bearing mice were intravenously injected with 1.25 mg/g of t-NP and treated + irradiation (at 10 Gy) using both preclinical and clinical radiation conditions. A total of 8 mice per group was used for preclinical radiations (220 kV), and 5 mice per group were used for the clinical radiation studies (6 MV). Animals were followed for ~180 days post-RT. Tumor sizes were monitored, and a size beyond ~2.5 cm (across any dimension) was considered terminal. Animals were euthanized as per institutional protocol. An additional cohort of $n = 3$ per group was sacrificed for tumor histological examination.

Functional imaging of tumor vascular modulation. Tumor blood vessels and nanoparticles were visualized using 3D-confocal imaging performed on a Zeiss 710 laser scanning confocal machine at 24 h post-administration. FITC-dextran (70 kDa; 60 μL of 1 mg/ml) was intravenously injected into Capan 1 tumor-bearing mice to label the functional tumor blood vessels. After 10–15 min, tumor was carefully dissected and glued to the bottom of a petri dish, immersed in PBS. Imaging was performed immediately on an upright Zeiss Examiner Z1 stand with a W-Plan Apochromatic 20x/NA 1.0 dipping objective. FITC excitation was performed using Argon laser at 488 nm and excitation of Alexa Fluor 647 tagged gold nanoparticles was performed with He-Ne laser at 633 nm. Fluorescence emission signals were detected using photomultiplier tubes. Z-stacks of the tissue volume were collected, and the 3D-reconstruction of tumor vasculature was carried out using Zeiss Zen software (Carl Zeiss Microscopy, Jena).

Bright light and TEM imaging of tumor neovasculature. Bright light imaging was performed on thin tumor tissue slices in order to visualize the cellular and vascular structures following toluidine blue staining. By adopting this method, single vessels were detected at higher magnifications (100x) using high-resolution transmission electron microscopy (Philips, Eindhoven, Netherlands). Tumor tissue pieces of 1 mm^3 were obtained from dissected whole tumor and fixed using a mixture of 2.5% glutaraldehyde in 0.2 M Sorensen buffer at pH: 7. Thin sections were sliced using ultracryotomy, followed by washing and staining with aqueous uranyl acetate (2%) for ~2 h. Tumor tissue was then placed at 4 °C under dark conditions. The tissue was further dehydrated by 100% ethanol and propylene oxide to be embedded in liquid epoxy resin. High-resolution electron microscopy was performed at different magnifications ranging from 2500x − 30000x to visualize tumor blood vessel damage pre and post-radiation therapy.

Histological examination. For histological evaluation, harvested tumor tissue was fixed in 2% formalin (neutral buffered) and embedded in paraffin. Thin tissue slices (~5 μm) were cut using cryotome, and the sections were mounted for antigen retrieval. Standard immunohistochemistry steps of deparaffinizing and rehydrating with various solvents was followed, and the immunostaining (Leica Bond automated stainer) was carried out. Primary and secondary antibodies were used for CD34 (Abcam ab8158 / 1:100 and HRP) and phosphohistone gammaH2AX: ser139 staining (Cell signaling technologies; #20E3 / 1:400). Sections were stained and counter-stained with Mayers hematoxylin. Following blocking and DAB steps, images were visualized using a Zeiss Axio Imager M2 microscope with a high-resolution Axiocam Mrm Rev.3 camera at 20x and 100x magnifications.

Image-guided drug delivery. To perform drug delivery studies, two different nanocarriers of 1–5 nm and 10–15 nm and circulation kinetics (1.5 h *vs*. 25 h) were used to perform both MR and optical imaging, respectively. Eight-week-old NCrFox-nu/nu mice weighing ~25 g were fed with standard food pellets and water ad libitum. Mice were housed in ventilated cages and placed in a clinically controlled room with customized treatment conditions. Capan-1 human pancreatic cancer cells ($5x10^6$ cells per 100 µL) were inoculated using subcutaneous injection into the right dorsolateral flank. A tumor size of ~6–8 mm^2 was obtained in ~8–9 weeks.

MRI studies using Gad-NC. Gadolinium based nanocarrier was intravenously administered (40 mM) to Capan-1 tumor bearing mice. DCE- and T2-weighted MRI (Bruker BioSpec 7 T, Bruker Corporation, Billerica, MA) was performed at 24 h post-radiation treatment at a dose of 10 Gy (240 kV). MRI was equipped with B-GA12S2 gradient and integrated to second order shim system which provides a maximum gradient amplitude of 440 mT/m and slew rate of 3440 T/m/s. The Bruker made 40 mm volume radiofrequency (RF) coil was used for both RF excitation and receiving. The Bruker AutoPac with laser positioning was used for the accurate registration of the region of interest. Animals were anesthetized using 1.5% isoflurane mixed with medical air and were maintained at a flow rate of 2 L/min. Respiratory gating was set-up using a pressure transducer placed on the abdomen of the animal.

T1-weighted MRI post-injection sequences. Gradient-Echo (GRE) T1-weighted, Magnetization-Prepared Rapid Gradient-Echo (MP-RAGE) T1-weighted, Dynamic Contrast Enhancement (DCE) with FLASH readout T1-weighted.

GRE T1-weighted parameters. TR = 245 ms, TE = 3.3 ms, FOV = 30 x 30 mm^2, matrix size = 192 x 192, spatial resolution = 117 x 156 μm^2, slice thickness = 0.5 mm, number of slices = 29, flip angle = 60 degrees' number of averages = 5, acquisition time = 3:54 min

MP-RAGE T1-weighted 3D method parameters. TR/TR_{eff} = 198.4 ms, TE = 2.2 ms, FOV = 30 x 30 x 30 mm^3, matrix size = 128 x 128 x 128, resolution = 234 x 234 x 234 μm^3, inversion time (TI) = 1700 ms, flip angle = 180/10 degrees, number of averages = 2, time = 8:27 min.

DCE T1-weighted parameters include. TR = 27.7 ms, TE = 2.2 ms, FOV = 30 x 30 mm^2, matrix size = 192 x 192, spatial resolution = 156 x 156 μm^2, slice thickness = 1 mm, number of slices = 5, number of repetitions = 90, flip angle = 30 degrees, number of averages = 5, time = 5:58 min.

MRI pre- Gad-NC administration sequences. GRE T1-weighted and (MP-RAGE) T1-weighted.

MRI data analysis. MRI signal to noise (SNR) image analysis intensity was performed using the Preclinical Imalytics (Gremse-IT, Aachen, Germany) for GRE and MP-RAGE T1-weighted data sets.

DCE-MRI (T1) maps were generated by the MIStar (Apollo Medical Imaging Technology, Australia) and Preclinical Imalytics (Gremse-IT, Aachen, Germany) image analysis software. The parameters such as vessel permeability (K_{trans}), extravascular back-flux (K_{ep}) and extracellular extravascular interstitial volume (V_e) were calculated.

Whole body fluorescence imaging of FL-NC. A hydroxypropylmethacrylate polymer constructs coupled with a near-infrared labeled fluorescent macromolecule (HPMA-FL) with an excitation/ emission wavelength of 674/699 nm was administered at a dose of 1 mg/g (equiv. 1%-wt. of dye) in 100 µL saline. Serial FLI was performed at 24 and 72 h post-RT using the IVIS Spectrum *In Vivo* Imaging System (PerkinElmer, Hopkinton MA). The peak FLI signal intensity within selected regions of interest (ROI) was quantified using the Living Image Software (PerkinElmer, Hopkinton MA), and expressed as photon flux (p/sec/cm^2/sr). Planar FLI images from each of the four treated groups are displayed in the results section with indicated normalized minimal and maximal thresholds.

Statistical analysis. Data are expressed as a mean ± standard deviation or standard error unless otherwise indicated. Statistical analyses and graphs were carried out using Prism (GraphPad Software, Inc., La Jolla, CA). The unpaired, two-tailed Student's *t*-test was used to determine significance between an experimental group and a control group with a value of $P \leq 0.05$ considered significant. For comparisons between multiple groups, simple one-way ANOVA test was used. Kaplan-Meier plots with log-rank (Mantel-Cox) tests were used for survival studies. *In vivo* experiments were performed with a minimum of $n = 5$ animals per group unless mentioned.

Supporting information. Energy spectra and DNA damage studies, cytotoxicity, AUC measurements, LIBS imaging and colocalization, histology depicting nanoparticle localization across the tumor endothelium, preclinical radiation-based survival studies and additional MR imaging videos are included in the Supplementary information.

Received: 18 June 2019; Accepted: 11 September 2019;

Published online: 01 November 2019

References

1. Blanco, E., Shen, H. & Ferrari, M. Principles of nanoparticle design for overcoming biological barriers to drug delivery. *Nat Biotechnol* **33**, 941–951, https://doi.org/10.1038/nbt.3330 (2015).
2. Jain, R. K. Barriers to drug delivery in solid tumors. *Sci Am* **271**, 58–65 (1994).
3. Chadha, A. S. *et al*. Recent Advances and Prospects for Multimodality Therapy in Pancreatic Cancer. *Semin Radiat Oncol* **26**, 320–337, https://doi.org/10.1016/j.semradonc.2016.05.002 (2016).
4. Siegel, R. L., Miller, K. D. & Jemal, A. Cancer Statistics, 2017. *CA Cancer J Clin* **67**, 7–30, https://doi.org/10.3322/caac.21387 (2017).

5. Ryan, D. P., Hong, T. S. & Bardeesy, N. Pancreatic adenocarcinoma. *N Engl J Med* **371**, 2140–2141, https://doi.org/10.1056/NEJMc1412266 (2014).
6. Feig, C. *et al.* The pancreas cancer microenvironment. *Clin Cancer Res* **18**, 4266–4276, https://doi.org/10.1158/1078-0432.CCR-11-3114 (2012).
7. Von Hoff, D. D. *et al.* Increased survival in pancreatic cancer with nab-paclitaxel plus gemcitabine. *N Engl J Med* **369**, 1691–1703, https://doi.org/10.1056/NEJMoa1304369 (2013).
8. Barenholz, Y. Doxil(R)–the first FDA-approved nano-drug: lessons learned. *J Control Release* **160**, 117–134, https://doi.org/10.1016/j.jconrel.2012.03.020 (2012).
9. O'Brien, M. E. *et al.* Reduced cardiotoxicity and comparable efficacy in a phase III trial of pegylated liposomal doxorubicin HCl (CAELYX/Doxil) versus conventional doxorubicin for first-line treatment of metastatic breast cancer. *Ann Oncol* **15**, 440–449 (2004).
10. Ibrahim, N. K. *et al.* Phase I and pharmacokinetic study of ABI-007, a Cremophor-free, protein-stabilized, nanoparticle formulation of paclitaxel. *Clin Cancer Res* **8**, 1038–1044 (2002).
11. Adiseshaiah, P. P., Crist, R. M., Hook, S. S. & McNeil, S. E. Nanomedicine strategies to overcome the pathophysiological barriers of pancreatic cancer. *Nat Rev Clin Oncol* **13**, 750–765, https://doi.org/10.1038/nrclinonc.2016.119 (2016).
12. Arap, W., Pasqualini, R. & Ruoslahti, E. Cancer treatment by targeted drug delivery to tumor vasculature in a mouse model. *Science* **279**, 377–380 (1998).
13. Siemann, D. W. & Horsman, M. R. Vascular targeted therapies in oncology. *Cell Tissue Res.* **335**, 241–254, https://doi.org/10.1007/s00441-008-0646-0 (2009).
14. Kunjachan, S. *et al.* Nanoparticle Mediated Tumor Vascular Disruption: A Novel Strategy in Radiation Therapy. *Nano Lett* **15**, 7488–7496, https://doi.org/10.1021/acs.nanolett.5b03073 (2015).
15. Stylianopoulos, T., Munn, L. L. & Jain, R. K. Reengineering the Tumor Vasculature: Improving Drug Delivery and Efficacy. *Trends Cancer* **4**, 258–259, https://doi.org/10.1016/j.trecan.2018.02.010 (2018).
16. Garcia-Barros, M. *et al.* Tumor response to radiotherapy regulated by endothelial cell apoptosis. *Science* **300**, 1155–1159, https://doi.org/10.1126/science.1082504 [doi];300/5622/1155 [pii] (2003).
17. Kunjachan, S. *et al.* Passive versus active tumor targeting using RGD- and NGR-modified polymeric nanomedicines. *Nano.Lett.* **14**, 972–981, https://doi.org/10.1021/nl404391r (2014).
18. Hainfeld, J. F., Dilmanian, F. A., Slatkin, D. N. & Smilowitz, H. M. Radiotherapy enhancement with gold nanoparticles. *J.Pharm. Pharmacol.* **60**, 977–985, https://doi.org/10.1211/jpp.60.8.0005 (2008).
19. Berbeco, R. I., Ngwa, W. & Makrigiorgos, G. M. Localized dose enhancement to tumor blood vessel endothelial cells via megavoltage X-rays and targeted gold nanoparticles: new potential for external beam radiotherapy. *Int.J.Radiat.Oncol.Biol.Phys.* **81**, 270–276, https://doi.org/10.1016/j.ijrobp.2010.10.022 (2011).
20. Antosh, M. P. *et al.* Enhancement of radiation effect on cancer cells by gold-pHLIP. *Proc Natl Acad Sci USA* **112**, 5372–5376, https://doi.org/10.1073/pnas.1501628112 (2015).
21. Libutti, S. K. *et al.* Phase I and pharmacokinetic studies of CYT-6091, a novel PEGylated colloidal gold-rhTNF nanomedicine. *Clin Cancer Res* **16**, 6139–6149, https://doi.org/10.1158/1078-0432.CCR-10-0978 (2010).
22. Thakor, A. S., Jokerst, J., Zavaleta, C., Massoud, T. F. & Gambhir, S. S. Gold nanoparticles: a revival in precious metal administration to patients. *Nano Lett* **11**, 4029–4036, https://doi.org/10.1021/nl202559p (2011).
23. Hainfeld, J. F., Smilowitz, H. M., O'Connor, M. J., Dilmanian, F. A. & Slatkin, D. N. Gold nanoparticle imaging and radiotherapy of brain tumors in mice. *Nanomedicine (Lond)* **8**, 1601–1609, https://doi.org/10.2217/nnm.12.165 (2013).
24. Thakor, A. S. *et al.* The fate and toxicity of Raman-active silica-gold nanoparticles in mice. *Sci Transl Med* **3**, 79ra33, https://doi.org/10.1126/scitranslmed.3001674 (2011).
25. Eustis, S. & el-Sayed, M. A. Why gold nanoparticles are more precious than pretty gold: noble metal surface plasmon resonance and its enhancement of the radiative and nonradiative properties of nanocrystals of different shapes. *Chem Soc Rev* **35**, 209–217, https://doi.org/10.1039/b514191e (2006).
26. Hainfeld, J. F., Slatkin, D. N., Smilowitz, H. M. The use of gold nanoparticles to enhance radiotherapy in mice. *Phys Med Biol* **49**, N309–315 (2004).
27. Kolosnjaj-Tabi, J. *et al.* The One Year Fate of Iron Oxide Coated Gold Nanoparticles in Mice. *ACS Nano*, https://doi.org/10.1021/acsnano.5b00042 (2015).
28. Connor, E. E., Mwamuka, J., Gole, A., Murphy, C. J. & Wyatt, M. D. Gold nanoparticles are taken up by human cells but do not cause acute cytotoxicity. *Small* **1**, 325–327, https://doi.org/10.1002/smll.200400093 (2005).
29. Ruoslahti, E., Bhatia, S. N. & Sailor, M. J. Targeting of drugs and nanoparticles to tumors. *J Cell Biol* **188**, 759–768, https://doi.org/10.1083/jcb.200910104 (2010).
30. Theek, B. *et al.* Sonoporation enhances liposome accumulation and penetration in tumors with low EPR. *J Control Release* **231**, 77–85, https://doi.org/10.1016/j.jconrel.2016.02.021 (2016).
31. Cabral, H. *et al.* Accumulation of sub-100 nm polymeric micelles in poorly permeable tumours depends on size. *Nat.Nanotechnol.* **6**, 815–823, doi:nnano.2011.166 [pii];https://doi.org/10.1038/nnano.2011.166 (2011).
32. Prabhakar, U. *et al.* Challenges and key considerations of the enhanced permeability and retention effect for nanomedicine drug delivery in oncology. *Cancer Res* **73**, 2412–2417, https://doi.org/10.1158/0008-5472.CAN-12-4561 (2013).
33. Kumar, R. *et al.* Third generation gold nanoplatform optimized for radiation therapy. *Transl.Cancer Res.* **2**, https://doi.org/10.3978/j.issn.2218-676X.2013.07.02 (2013).
34. Yi, Y. *et al.* Targeted systemic delivery of siRNA to cervical cancer model using cyclic RGD-installed unimer polyion complex-assembled gold nanoparticles. *J Control Release* **244**, 247–256, https://doi.org/10.1016/j.jconrel.2016.08.041 (2016).
35. Krishnan, S. *et al.* Focal Radiation Therapy Dose Escalation Improves Overall Survival in Locally Advanced Pancreatic Cancer Patients Receiving Induction Chemotherapy and Consolidative Chemoradiation. *Int J Radiat Oncol Biol Phys* **94**, 755–765, https://doi.org/10.1016/j.ijrobp.2015.12.003 (2016).
36. Ma, X. *et al.* Colloidal Gold Nanoparticles Induce Changes in Cellular and Subcellular Morphology. *ACS Nano* **11**, 7807–7820, https://doi.org/10.1021/acsnano.7b01760 (2017).
37. Hirn, S. *et al.* Particle size-dependent and surface charge-dependent biodistribution of gold nanoparticles after intravenous administration. *Eur.J.Pharm.Biopharm.* **77**, 407–416, S0939-6411(10)00370-X [pii]; https://doi.org/10.1016/j.ejpb.2010.12.029 (2011).
38. Heinrich, A. K. *et al.* Improved Tumor-Specific Drug Accumulation by Polymer Therapeutics with pH-Sensitive Drug Release Overcomes Chemotherapy Resistance. *Mol Cancer Ther* **15**, 998–1007, https://doi.org/10.1158/1535-7163.MCT-15-0824 (2016).
39. Kunjachan, S. *et al.* Noninvasive optical imaging of nanomedicine biodistribution. *ACS Nano* **7**, 252–262, https://doi.org/10.1021/nn303955n (2013).
40. Pike, D. B. & Ghandehari, H. HPMA copolymer-cyclic RGD conjugates for tumor targeting. *Adv Drug Deliv Rev* **62**, 167–183, https://doi.org/10.1016/j.addr.2009.11.027 (2010).
41. Detappe, A. *et al.* Advanced multimodal nanoparticles delay tumor progression with clinical radiation therapy. *J Control Release* **238**, 103–113, https://doi.org/10.1016/j.jconrel.2016.07.021 (2016).
42. Verry, C. *et al.* MRI-guided clinical 6-MV radiosensitization of glioma using a unique gadolinium-based nanoparticles injection. *Nanomedicine (Lond)* **11**, 2405–2417, https://doi.org/10.2217/nnm-2016-0203 (2016).

43. Chytil, P. *et al*. Dual fluorescent HPMA copolymers for passive tumor targeting with pH-sensitive drug release II: impact of release rate on biodistribution. *J Control Release* **172**, 504–512, https://doi.org/10.1016/j.jconrel.2013.05.008 (2013).
44. Kunjachan, S., Ehling, J., Storm, G., Kiessling, F. & Lammers, T. Noninvasive Imaging of Nanomedicines and Nanotheranostics: Principles, Progress, and Prospects. *Chem Rev*, https://doi.org/10.1021/cr500314d (2015).
45. Mignot, A. *et al*. A top-down synthesis route to ultrasmall multifunctional Gd-based silica nanoparticles for theranostic applications. *Chemistry* **19**, 6122–6136, https://doi.org/10.1002/chem.201203003 (2013).
46. Lux, F. *et al*. Ultrasmall rigid particles as multimodal probes for medical applications. *Angew Chem Int Ed Engl* **50**, 12299–12303, https://doi.org/10.1002/anie.201104104 (2011).
47. Ulbrich, K. *et al*. Polymeric drugs based on conjugates of synthetic and natural macromolecules. I. Synthesis and physico-chemical characterisation. *J Control Release* **64**, 63–79 (2000).
48. Chytil, P., Etrych, T., Kriz, J., Subr, V. & Ulbrich, K. N-(2-Hydroxypropyl)methacrylamide-based polymer conjugates with pH-controlled activation of doxorubicin for cell-specific or passive tumour targeting. Synthesis by RAFT polymerisation and physicochemical characterisation. *Eur J Pharm Sci* **41**, 473–482, https://doi.org/10.1016/j.ejps.2010.08.003 (2010).
49. Pan, Y., Wu, Q., Qin, L., Cai, J. & Du, B. Gold nanoparticles inhibit VEGF165-induced migration and tube formation of endothelial cells via the Akt pathway. *Biomed Res Int* **2014**, 418624, https://doi.org/10.1155/2014/418624 (2014).

Acknowledgements

We greatly acknowledge the efforts by histology core at Brigham and Women's Hospital and Harvard Medical School, and the TEM core facility at Harvard Medical School. We thank Anirudha Karve (NCI) for technical assistance with small animal radiation therapy platform and Francesco Pelascini (CRITT Matériaux Alsace) for the technical assistance with epoxy-embedding and LIBS imaging of biological tissue samples. This project was supported, in part, by a grant from the JCRT foundation and by award number R21CA188633 from the National Cancer Institute (NCI). The content of this manuscript is solely the responsibility of the authors and does not necessarily reflect or represent the official views of the NCI or NIH. This collaborative project was also supported by funding from Czech Science Foundation grant 16–17207 S and the Ministry of Health of the Czech Republic grant 16-28594 A. Shady Kotb received financial assistance through the "Investissement d'Avenir" (ANR-11-IDEX-0063) program from the LABEX PRIMES of Lyon 1 University, France.

Author contributions

S.K. and R.I.B. designed the study. S.K., R.P., M.P., R.K., B.S., F.G., P.T., F.T., V.M.R., L.S., A.D., S.Y.K., A.P., I.S. and T.I. conducted the research. S.K. analyzed the data. S.K., G.M.M. and T.E. collaborated on this research. S.K., G.M.M. and R.I.B. discussed and finalized the content of this manuscript.

Competing interests

The authors declare no competing interests.

Additional information

Supplementary information is available for this paper at https://doi.org/10.1038/s41598-019-50538-w.

Correspondence and requests for materials should be addressed to S.K.

Reprints and permission information is available at www.nature.com/reprints.

Publisher's note Springer Nature remains neutral with regard to jurisdictional claims in published maps and institutional affiliations.